

CANCER

Structure-based design of small-molecule inhibitors of EBNA1 DNA binding blocks Epstein-Barr virus latent infection and tumor growth

Troy E. Messick^{1*}, Garry R. Smith², Samantha S. Soldan¹, Mark E. McDonnell^{2,3}, Julianna S. Deakyne¹, Kimberly A. Malecka¹, Lois Tolvinski¹, A. Pieter J. van den Heuvel³, Bai-Wei Gu³, Joel A. Cassel³, Donna H. Tran¹, Benjamin R. Wassermann¹, Yan Zhang², Venkata Velvadapu², Edward R. Zartler⁴, Pierre Busson⁵, Allen B. Reitz², Paul M. Lieberman^{1*}

Epstein-Barr virus (EBV) is a DNA tumor virus responsible for 1 to 2% of human cancers including subtypes of Burkitt's lymphoma, Hodgkin's lymphoma, gastric carcinoma, and nasopharyngeal carcinoma (NPC). Persistent latent infection drives EBV-associated tumorigenesis. Epstein-Barr nuclear antigen 1 (EBNA1) is the only viral protein consistently expressed in all EBV-associated tumors and is therefore an attractive target for therapeutic intervention. It is a multifunctional DNA binding protein critical for viral replication, genome maintenance, viral gene expression, and host cell survival. Using a fragment-based approach and x-ray crystallography, we identify a 2,3-disubstituted benzoic acid series that selectively inhibits the DNA binding activity of EBNA1. We characterize these inhibitors biochemically and in cell-based assays, including chromatin immunoprecipitation and DNA replication assays. In addition, we demonstrate the potency of EBNA1 inhibitors to suppress tumor growth in several EBV-dependent xenograft models, including patient-derived xenografts for NPC. These inhibitors selectively block EBV gene transcription and alter the cellular transforming growth factor-β (TGF-β) signaling pathway in NPC tumor xenografts. These EBNA1-specific inhibitors show favorable pharmacological properties and have the potential to be further developed for the treatment of EBV-associated malignancies.

INTRODUCTION

Epstein-Barr virus (EBV) is a human gammaherpesvirus that establishes lifelong latent infection in more than 90% of the adult population [reviewed in (1–4)]. Latent EBV infection is the causative agent of a wide range of human cancers of epithelial, mesenchymal, and lymphocytic origin, including forms of Burkitt's lymphoma, nasopharyngeal carcinoma (NPC), Hodgkin's lymphoma, gastric carcinoma, and angiogenic T/natural killer cell lymphoma (2, 5). During latency, EBV expresses a limited set of genes that stimulate cellular proliferation and promote survival of the latently infected host cell. Although clinically available inhibitors of herpesvirus DNA polymerases, such as acyclovir and phosphonoacetic acid, have partial inhibitory activity against EBV lytic replication, no existing pharmacological agent selectively targets EBV latency. Chief among the latency genes is Epstein-Barr nuclear antigen 1 (EBNA1), which is consistently expressed in all EBV-positive tumors (5–7). EBNA1 is a sequence-specific DNA binding protein that binds to the viral origin of plasmid replication (OriP) and is required for viral DNA replication and episome maintenance during latent infection in proliferating cells (8, 9). EBNA1 also confers transcriptional control of viral latency genes and enhances infected cell survival and immortalization of primary B lymphocytes (6, 10, 11). The DNA binding domain (DBD) is required for all known functions of EBNA1. The three-dimensional (3D) structure of EBNA1 bound to

its cognate DNA sequence has been solved by x-ray crystallography, showing structural homology to related viral proteins, including human papillomavirus (HPV) E2 and Kaposi's sarcoma-associated herpesvirus (KSHV) latency-associated nuclear antigen (LANA), but not to human proteins (12, 13). The crystal structure also revealed considerable opportunity for the development of small-molecule inhibitors that block EBNA1 DBD function.

RESULTS

Crystal structures of fragments bound to EBNA1 reveal a pocket important for DNA binding

To develop selective small-molecule inhibitors of EBNA1, we used a fragment-based approach to identify starting points for medicinal chemistry (14). One thousand five hundred fragments from the Maybridge Fragment Library were docked into a DNA binding region using Molegro (CLC bio). One hundred fragments of the in silico hit compounds were selected, pooled in groups of five, and soaked into EBNA1 crystals. We observed at least one compound in 18 datasets and categorized these fragments into binding sites 1 to 4 (Fig. 1A). The high resolution of the x-ray diffraction datasets facilitated the identification of specific fragments in the crystal structures. None of the compounds bound in the site predicted by the docking algorithm. Site 1 contained five fragments that bound in a shallow region at the DNA interface; site 2 contained 12 fragments that bound to a region that also makes critical contacts with the DNA; site 3 contained one fragment in close proximity to the dimer interface; and site 4 contained two fragments that were distant from the DNA binding surface.

Several features of the site 2 fragments made them attractive for further medicinal chemistry work (Fig. 1B). All fragments contained

Copyright © 2019
The Authors, some
rights reserved;
exclusive licensee
American Association
for the Advancement
of Science. No claim
to original U.S.
Government Works

¹The Wistar Institute, 3601 Spruce Street, Philadelphia, PA 19104, USA. ²Fox Chase Chemical Diversity Center Inc., 3805 Old Easton Road, Doylestown, PA 18902, USA.

³Vironika LLC, 3624 Market Street, Ste 5E, Philadelphia, PA 19104, USA. ⁴Quantum Tessera Consulting LLC, 508 Tawnyberry Lane, Collegeville, PA 19426, USA. ⁵Institut Gustave Roussy, 114 Rue Edouard Vaillant, 94800 Villejuif, France.

*Corresponding author. Email: lieberman@wistar.org (P.M.L.); troymessick@gmail.com (T.E.M.)

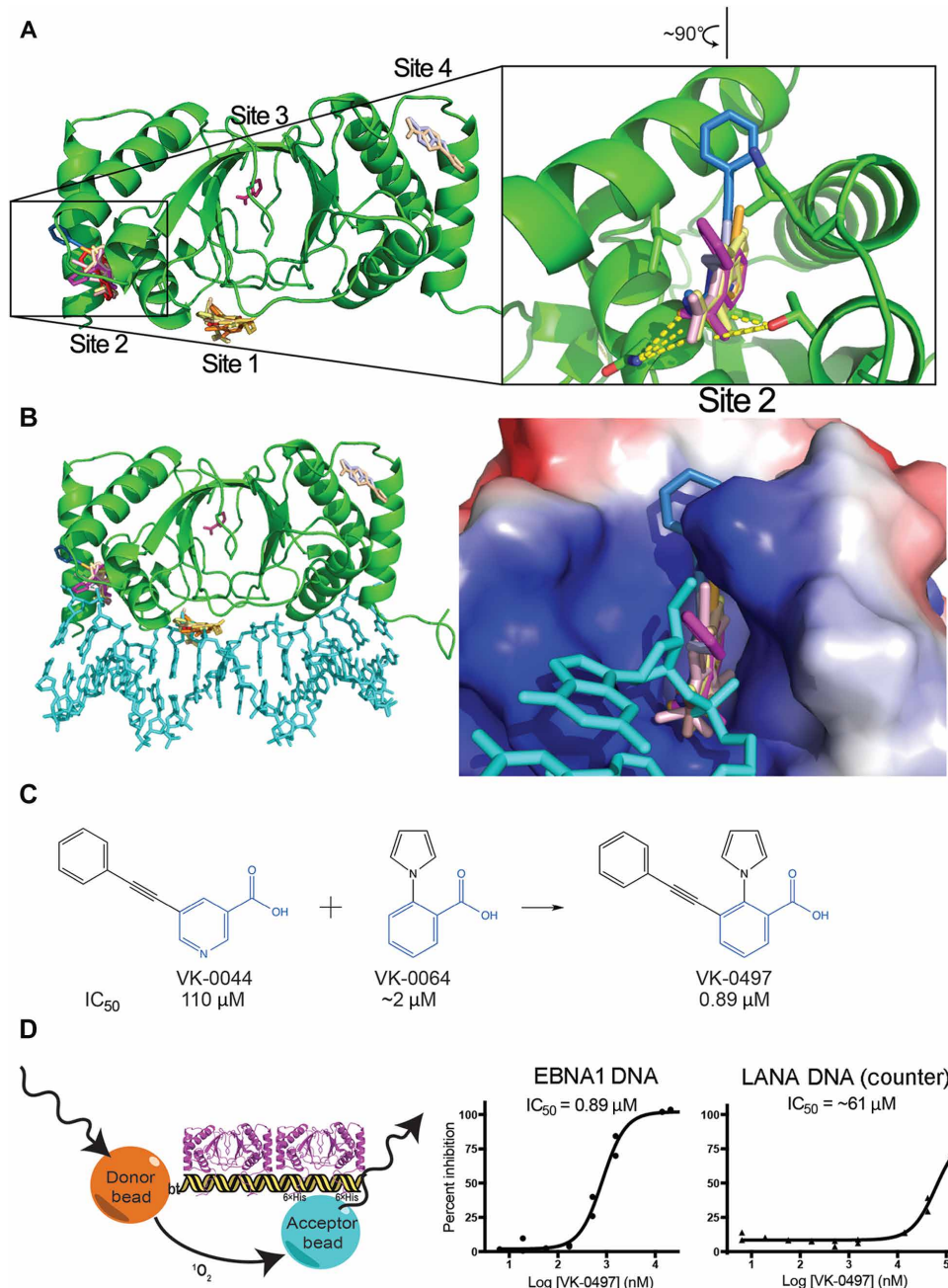


Fig. 1. Structure-guided fragment-based drug design for inhibitors of EBNA1 DNA binding function. (A) Superimposition of x-ray crystal structures for 20 fragments bound to four different sites in the EBNA1 DBD (green ribbon). Right inset: Close-up and 90° turn showing fragments bound to site 2. (B) Same as in (A), with modeled superposition of cognate DNA bound to EBNA1. Right inset: Space-filling model colored according to electrostatic potential of EBNA1 with fragments bound to site 2. (C) Fragments VK-0044 [median inhibitory concentration (IC_{50}), 110 μ M] and VK-0064 (IC_{50} , 2 μ M) were chemically merged to generate a more potent core scaffold VK-0497 (IC_{50} , 0.89 μ M). (D) Schematic of ALPHA proximity assay for EBNA1 binding to its cognate DNA showing ~60-fold selectivity relative to counterscreen for LANA binding to its cognate DNA (right panel).

a five- or six-membered ring that occupied a deep hydrophobic pocket in EBNA1. Ten of the 12 fragments contained an acidic moiety (either a carboxylic acid or tetrazole) that made hydrogen bond contacts with Asn⁵¹⁹ and Thr⁵⁹⁰. Superimposing the DNA bound structure revealed that these residues make critical interactions with

the DNA backbone (Fig. 1, A and B). We predicted that an acidic group at that position would sterically interfere with the ability of EBNA1 to bind the DNA phosphate. We noted that fragments containing nicotinic acid and benzoic acid overlapped in both the hydrophobic and acidic regions. We therefore merged these two fragments, the 5-phenylacetylenyl nicotinic acid (VK-0044) and 2-pyrrolo-benzoic acid (VK-0064), to create 2-pyrrolo-3-phenylacetylenyl benzoic acid (VK-0497) (Fig. 1C).

The activity of these fragments was measured in biochemical assays for inhibition of EBNA1 DNA binding. We first used a high-throughput ALPHA proximity DNA binding assay with His-tagged EBNA1 linked to nickel donor beads and biotinylated DNA linked to streptavidin-coated acceptor beads (Fig. 1D). When the complex between EBNA1 and DNA was challenged with an inhibitor, we observed a loss in signal emitted from the acceptor bead. The merged fragment was found to have >10-fold increase in potency relative to the individual fragments and reached submicromolar activity. The counter-screen assay with His-tag LANA binding to its cognate DNA sequence demonstrated ~60-fold selectivity (Fig. 1D).

We determined the cocrystal structure of VK-0497 and observed complementarity between the shape and charge distribution of the inhibitor and the EBNA1 pocket (Fig. 2A, fig. S1, and table S1) (15). EBNA1 forms a concave surface around VK-0497 with the central phenyl ring in a deep hydrophobic pocket. The acetylene threads the molecule from this pocket through a tunnel bounded by the aliphatic side-chain atoms of Lys⁵⁸⁶ to a solvent-exposed region. We observed two cation-π interactions that sandwich the electron-rich pyrrole between two lysine residues, Lys⁴⁷⁷ and Lys⁵⁸⁶. Lys⁴⁷⁷, Asn⁵¹⁹, and Thr⁵⁹⁰ formed a network of hydrogen-bonding contacts with the carboxylic acid.

With respect to medicinal chemistry, the high electron density of the pyrrole ring found in VK-0497 is a metabolic liability. Therefore, we replaced the pyrrole ring with a 6-indolyl group (VK-0941). We developed a DNA-independent competition assay using a biotinylated version of VK-0941 (VK-2114) as a reference probe in an ALPHA assay with EBNA1 (Fig. 2B). Nonbiotinylated VK-0941 displaced

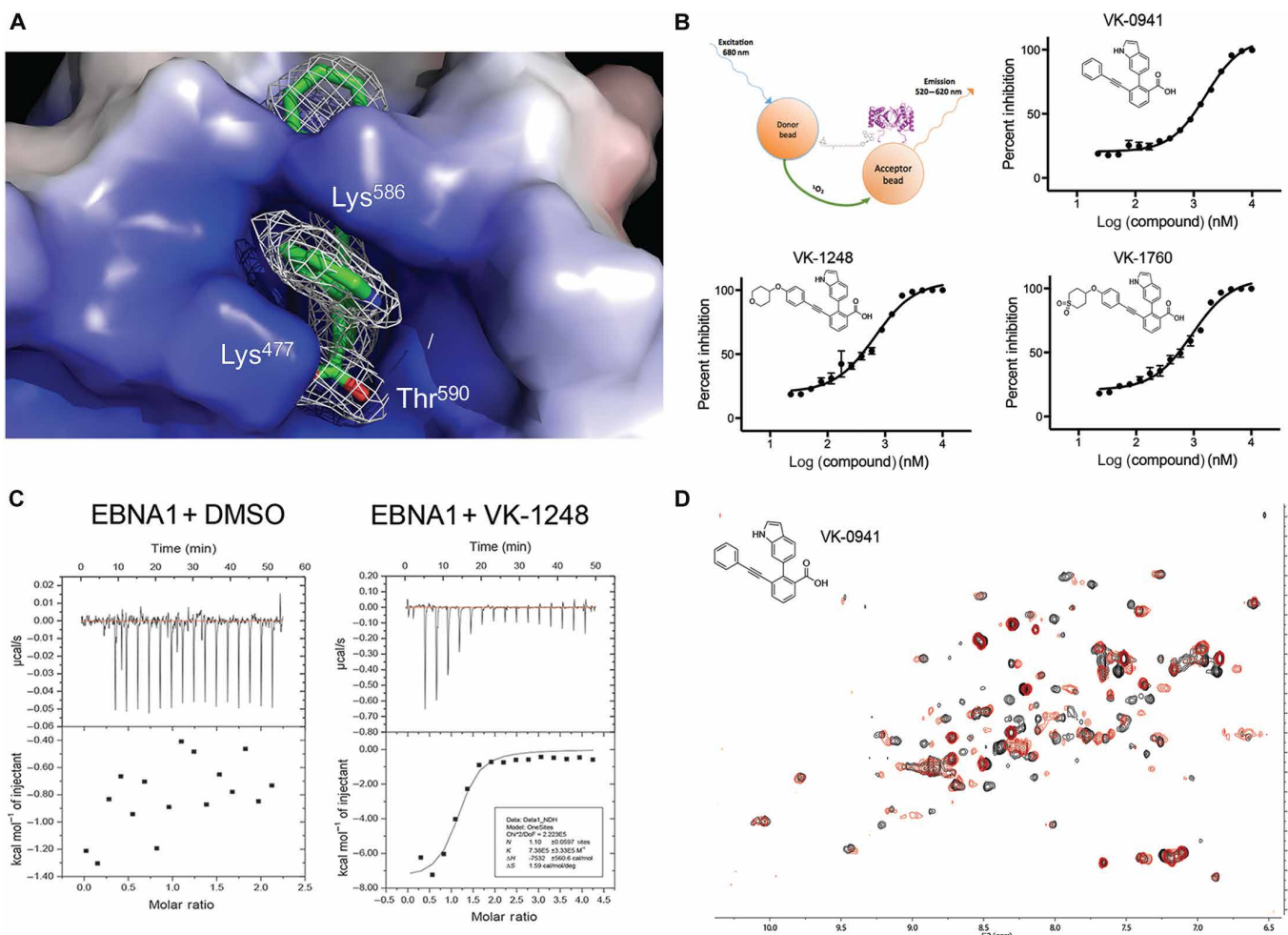


Fig. 2. Biochemical and biophysical basis for EBNA1 inhibitors. (A) X-ray crystal structure of VK-0941 bound to EBNA1 with amino acid residues involved in hydrogen-bonding contacts. (B) Schematic for ALPHA competition assay using biotin linker-conjugated VK-0941 used for the assessment of more potent compounds VK-1248 and VK-1760. (C) Isothermal titration calorimetry (ITC) isotherms of EBNA1 with dimethyl sulfoxide (DMSO) and VK-1248. (D) Heteronuclear single-quantum coherence (HSQC) nuclear magnetic resonance (NMR) spectra of ¹⁵N-labeled EBNA1 unbound (black) and bound with VK-0941 (red). ppm, parts per million.

VK-2114 binding to EBNA1 with an IC₅₀ of 0.927 μM. On the basis of the structure of VK-0941 bound to EBNA1, a region beyond the phenyl acetylene became the focus of further medicinal chemistry optimization. Two attractive compounds, VK-1248 (oxy-4-tetrahydropyran) and VK-1760 (oxy-4-tetrahydrothiopyran-dioxide), had IC₅₀ values of 0.388 and 0.713 μM, respectively, in the ALPHA assay. Both were shown to bind EBNA1 similarly to VK-0941 by x-ray crystallography (figs. S2 and S3). VK-1760 makes additional productive contacts with Asn⁴⁸⁰ and Arg⁴⁹¹, which may account for increased binding affinity.

We next validated EBNA1 inhibitor binding using various orthogonal biochemical assays. We determined the affinity of compounds with immobilized EBNA1 using surface plasmon resonance and characterized binding kinetics for VK-1760 with a K_d (dissociation constant) of 2.5 μM and k_{off} of 0.0053 s⁻¹ (figs. S4 and S5). The direct binding of VK-1248 was also demonstrated using ITC, which revealed a K_d of 1.4 ± 3.0 μM (Fig. 2C); this binding is primarily driven by enthalpic terms with a ΔH° of -31.5 ± 2.3 kJ/mol, a ΔS° of 6 kJ/mol K, and a ~1:1 stoichiometry. Last, using HSQC NMR experi-

ment and ¹⁵N-labeled EBNA1 protein, we observed direct binding of VK-0497 and VK-0941 to EBNA1 (Fig. 2D and fig. S6). Upon inhibitor addition, we observed chemical shifts in the spectra (red) relative to the absence of ligand (black) with changes in asparagine or lysine residues consistent with our x-ray crystallography data.

EBNA1 inhibitors are active in cell-based assays

For cell-based assays, the carboxylic acids in VK-1248 and VK-1760 are known to limit cell penetrance (16) and were therefore converted to their prodrug methyl esters VK-1727 and VK-1850, respectively (Fig. 3A). Prodrug methyl esters can be readily converted to the acid form by cellular esterases (17). VK-1727 and VK-1850 were tested for activity in cell proliferation assays measuring 5-bromo-2'-deoxyuridine (BrdU) incorporation and found to selectively inhibit proliferation of EBV-positive cells but not similarly growing EBV-negative cells (Fig. 3B and data file S1). Similar selectivity was observed using a resazurin assay that measures cellular metabolism (Fig. 3C and fig. S7). The acid versions of these compounds, VK-1248 and VK-1760, had no measurable activity in these cell-based

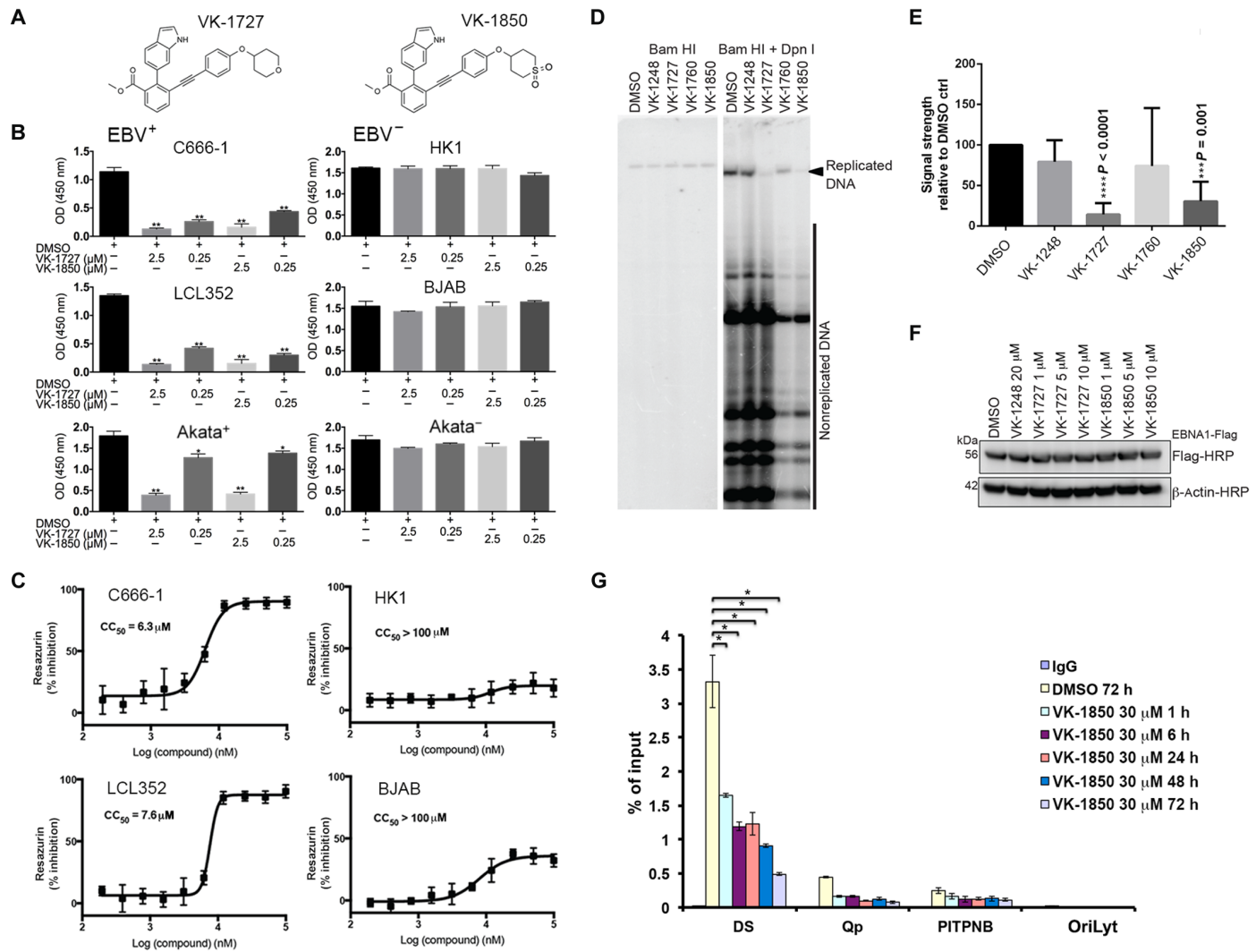


Fig. 3. Cell-based assay validation for EBNA1 inhibition. (A) Chemical structures of methyl esters of VK-1760 (VK-1850) and VK-1248 (VK-1727) used for in vitro cell-based assays. (B) BrdU proliferation assays for EBV-positive cell lines (C666-1, LCL352, and Akata⁺) compared to EBV-negative cell lines (HK1, BJAB, and Akata⁻). Cells were treated with DMSO control or VK-1727 or VK-1850 at 0.25 or 2.5 μM for 2 days with fresh drug and medium change each day. OD, optical density. (C) Resazurin cell viability assay for EBV-positive cells (C666-1 and LCL352) or EBV-negative cells (HK1 and BJAB) with 10-point median effective concentration (EC_{50}) calculation for VK-1727. (D) EBNA1-dependent OriP replication assays in transiently transfected cells treated with either DMSO or 10 μM VK-1248, VK-1727, VK-1760, or VK-1850. Dpn I-resistant replicated DNA is indicated by an arrowhead. (E) Average replication activity for three independent DNA replication assays of EBNA1 in the presence of inhibitors after transient transfection in 293T, HeLa, and SUNE1 cells averaged together and normalized to DMSO controls. P values were determined by two-tailed Student's t test. (F) Representative Western blot of EBNA1 and actin after treatment with increasing amounts of inhibitors 4 days after transfection. HRP, horseradish peroxidase. (G) ChIP assay for EBNA1 binding to the DS, Qp, PITPNB cellular locus, or negative control EBV OriLyt locus in EBV-positive C666-1 NPC cells treated with DMSO or 30 μM VK-1850 for times ranging from 1 to 72 hours. P values were determined by two-tailed Student's t test for three biological replicates. * P < 0.01. IgG, immunoglobulin G.

assays (fig. S8 and data file S2). We next assayed VK-1727 and VK-1850, along with their acid analogs VK-1248 and VK-1760, for their ability to inhibit EBNA1-dependent DNA replication from an OriP-containing plasmid (Fig. 3D). We observed that methyl esters VK-1727 and VK-1850 were potent inhibitors of EBNA1-dependent OriP DNA replication, whereas corresponding carboxylic acids VK-1248 and VK-1760 had only partial inhibitory activity, as expected (Fig. 3E and data file S3). None of the compounds decreased EBNA1 protein expression (Fig. 3F). To determine whether compounds were interfering with EBNA1 DNA binding function in vivo, we performed a chromatin immunoprecipitation (ChIP) assay in an EBV-positive NPC cell line, C666-1 (Fig. 3G and data file S4).

Treatment with 30 μM VK-1850 significantly (P < 0.01) reduced EBNA1 binding to the viral dyad symmetry (DS) and other EBNA1 binding sites, including the EBV Qp and cellular binding site at the PITPNB gene within 1 hour of treatment (Fig. 3G). As expected, no EBNA1 binding was observed at the negative control region OriLyt.

EBNA1 inhibitors block EBV tumor growth in vivo

To assess the efficacy of EBNA1 inhibitors in vivo, we used several different EBV-dependent xenograft models: one lymphoma model [lymphoblastoid cell line (LCL)], one NPC cell line (C666-1), and two NPC patient-derived xenograft (PDX) models (C15 and C17) (Fig. 4)

(18, 19). We first used an EBV-positive, bioluminescence-based mouse model using an LCL-expressing green fluorescent protein (GFP)–luciferase transgene (designated M14). M14 cells were engrafted into the flanks of NSG-SCID (NOD.Cg-*Prkdc*^{scid} *Il2rgtm1Wjl*/SzJ) mice, and tumor size was monitored by both bioluminescence and

caliper measurements (Fig. 4, A to C). VK-1727 and VK-1850 (10 mg/kg, intraperitoneally) provided significant ($P < 0.0001$) tumor growth inhibition (TGI) (88.3 and 91.3% TGI, respectively) compared to vehicle control (Fig. 4, B and C). For the NPC models, we used the C666-1 cell line (Fig. 4D) and two patient-derived tumor lines, C15-PDX

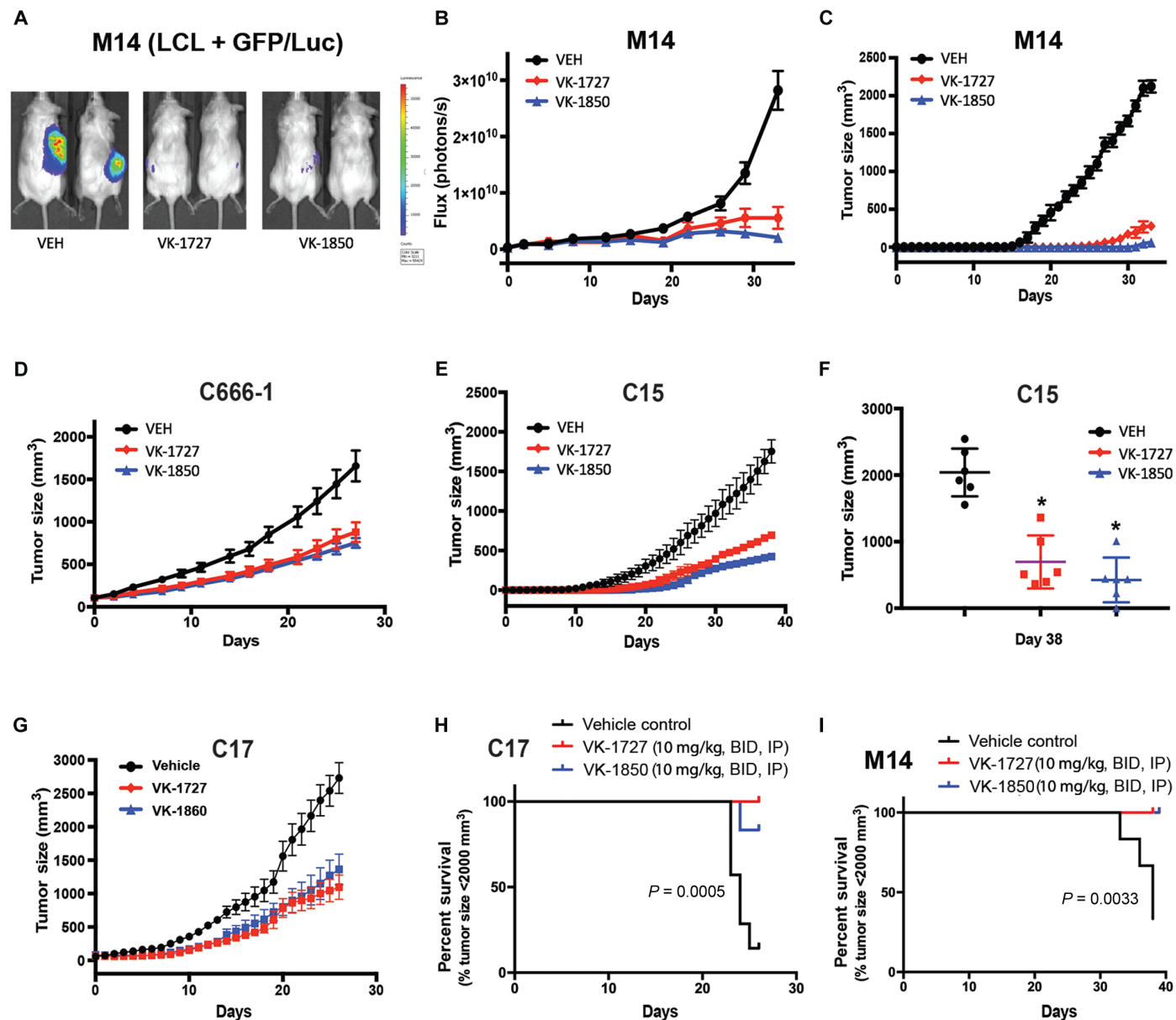


Fig. 4. EBNA1 inhibitors and EBV-positive tumor growth. (A to C) NSG-SCID ($n = 10$ per group) mice injected with 10^6 M14 LCLs expressing luciferase were treated twice daily (BID) with VK-1727 (10 mg/kg; red), VK-1850 (10 mg/kg; blue), or vehicle (black) and monitored for (A) bioluminescence that was (B) quantified (flux; photons/s) with a Xenogen IVIS imager and for (C) tumor size measured by calipers. Tumor growth was significantly ($P < 0.0001$, Kruskal-Wallis test) inhibited in mice treated with EBNA1 inhibitors as measured by both bioluminescence and tumor size. (D) Beige-SCID mice ($n = 8$ per group) were injected with the EBV-positive NPC cell line C666-1, which was allowed to grow to 100 mm^3 , and then treated twice daily with vehicle (black), VK-1727 (10 mg/kg; red), or VK-1850 (10 mg/kg, blue) and monitored by caliper measurement. NPC tumor growth was significantly ($P = 0.0035$, Kruskal-Wallis test) inhibited in mice treated with EBNA1 inhibitors. (E) Athymic Swiss nude mice ($n = 6$ per group) were surgically engrafted with C15-PDX and treated twice daily with vehicle control (black), VK-1727 (10 mg/kg; red), or VK-1850 (10 mg/kg; blue) and monitored by caliper measurement. (F) Tumor growth for C15-PDX shown in (E) was significantly ($P < 0.0001$, Kruskal-Wallis test) inhibited in mice treated with VK-1727 and VK-1850. * $P < 0.05$. (G) Athymic Swiss nude mice ($n = 6$ per group) were surgically engrafted with C17-PDX and treated twice daily with vehicle control (black), VK-1727 (10 mg/kg; red), or VK-1850 (10 mg/kg; blue) and monitored by caliper measurement. (H) Survival curve for C17-PDX animals shown in (G). $P = 0.0005$, log-rank Mantel-Cox test. (I) Survival curve for NSG mice implanted with M14 tumors and treated with EBNA1 inhibitor or vehicle until tumor reached 2000 mm^3 ($P = 0.0005$, log-rank Mantel-Cox test). IP, intraperitoneally.

(Fig. 4, E and F) and C17-PDX (Fig. 4, G and H). C666-1 cells were injected into the flanks of mice, whereas PDX tumors were serially transplanted in mice and allowed to grow to palpable size before drug treatment. Treatment with VK-1727 and VK-1850 (10 mg/kg) provided significant ($P < 0.0001$) TGI for all NPC models, showing 67 and 70% TGI, respectively, for C15-PDX (Fig. 4F). Prolonged survival was demonstrated for treatment of C17 (Fig. 4H) and M14 (Fig. 4I) with VK-1727 or VK-1850 (10 mg/kg). EBNA1 inhibitors did not affect an EBV-negative A549 tumor growth (Fig. 5), indicating selectivity for EBV-infected tumors.

EBNA1 inhibitors have therapeutic potential

Clinically, NPC tumors are treated initially with γ -irradiation (IR), followed by cisplatin and 5-fluorouracil (5-FU) (20). We found that VK-1850 provided more robust TGI for C15-PDX and C17-PDX tumor relative to weekly treatment with 4-Gy IR and further reduced tumor growth when combined with IR (Fig. 6, A and B, and fig. S9) or with cisplatin (fig. S10). VK-1850 (at 10 mg/kg) provided greater tumor inhibition than standard doses of several other anti-neoplastic pharmacological agents, including a poly(ADP-ribose) polymerase (PARP) inhibitor (olaparib), a phosphatidylinositol 3-kinase (PI3K) inhibitor (idelalisib), and 5-FU (Fig. 6C). We also found that the prodrug methyl ester VK-1850 is efficiently converted to active acid VK-1760 and accumulates in NPC tumors, indicating

a favorable pharmacological profile (Fig. 6D and fig. S11). Prolonged treatment (8 weeks) of EBV-positive Akata or M14 led to a decrease of 40 to 70% of the EBV copy number relative to untreated controls (fig. S12A and data file S5). Response to EBNA1 inhibitors was essentially unchanged after long-term treatment of EBV-positive Akata cells and diminished by ~5% in M14 (fig. S12B and data file S6). These findings suggest that EBNA1 inhibitors reduce EBV DNA copy number without causing drug resistance.

EBNA1 inhibitors affect the expression of viral and cellular genes in vivo

To understand the effects of EBNA1 inhibition on cellular and viral gene expression, we isolated RNA from residual tumor material upon completion of the C15-PDX experiment and submitted them for gene expression analysis (Fig. 7, A to C) using the PanCancer Pathways Panel of 700 human genes (NanoString Technologies) supplemented with an analysis of ~30 EBV-expressed genes. Comparison of the vehicle-treated and the VK-1727- or VK-1850-treated mice demonstrated that the expression of EBV-encoded genes, including those coding for EBNA1, EBNA2, LMP1, and ZTA, was lower in tumors treated with an EBNA1 inhibitor (Fig. 7, A and B). Cellular gene pathways for transforming growth factor- β (TGF- β), signal transducer and activator of transcription (STAT), and mitogen-activated protein kinase (MAPK) were also affected by EBNA1 inhibitor treatment (Fig. 7C, fig. S13, and data files S7 and S8). The time-dependent effect of VK-1850 was measured by Epstein-Barr-encoded RNA (EBER)-in situ hybridization (ISH) on M14 tumors at days 1 to 10 and revealed a strong reduction in EBER signal in drug-treated tumor tissue sections by 3 and 6 days after treatment (Fig. 7D). Collectively, these results suggest that pharmacological inhibition of EBNA1 has rapid and profound effects on EBV and cellular gene expression, correlating with loss of EBV genomes and a suppression in EBV-driven tumor cell growth pathways.

DISCUSSION

Latent infection with EBV results in the expression of viral genes that can drive cellular proliferation and oncogenesis. EBNA1 has been recognized as an attractive target for elimination of latent infection and treatment of EBV-associated disease because of its role in the immortalization of primary B lymphocytes, the stable maintenance of the EBV genome during latent infection, and its universal presence in EBV-positive tumors. Others have also developed methods, both biological and pharmacological, to target EBNA1 to treat EBV-associated disease (21–26). Interrogation of the crystal structure of the EBNA1 DBD with a fragment-based approach revealed a vulnerable surface within its DNA binding interface, enabling us to develop a series of inhibitors of EBNA1 DNA binding activity that have high potency in biochemical inhibitor assays and high selectivity in multiple cell-based assays. Xenograft studies using EBV-positive NPC and LCLs have shown that these EBNA1 inhibitors successfully inhibit tumor growth and expression of EBV RNA, affect multiple cancer pathways in vivo, and have favorable pharmacological properties, underscoring the potential use of small-molecule EBNA1 inhibitors in a multitude of EBV-driven malignancies.

We propose that the mechanism of action for the EBNA1 inhibitors described in this study is through the disruption of stable EBNA1 DNA binding. Superimposing the crystal structures of EBNA1 bound to inhibitors with the crystal structure of EBNA1

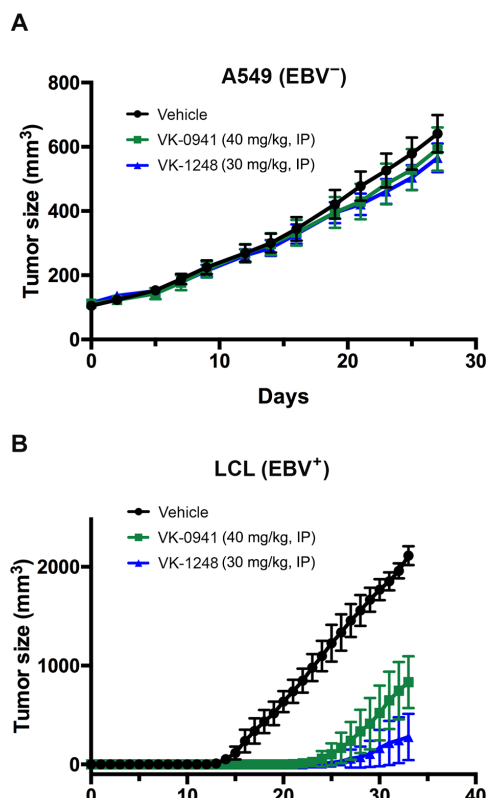


Fig. 5. EBNA1 inhibitors and EBV-negative tumor growth. (A) Mice engrafted with EBV-negative lung carcinoma cell line A549 were treated twice daily with VK-0941 (40 mg/kg), VK-1248 (30 mg/kg), or vehicle. (B) Mice engrafted with EBV-positive LCLs were treated twice daily with VK-0941 (30 mg/kg), VK-1248 (30 mg/kg), or vehicle. Tumor size was significantly decreased in EBV-positive LCLs treated with EBNA1 inhibitors [$P < 0.0001$, ordinary one-way analysis of variance (ANOVA)] but not in the EBV-negative A549 cell line.

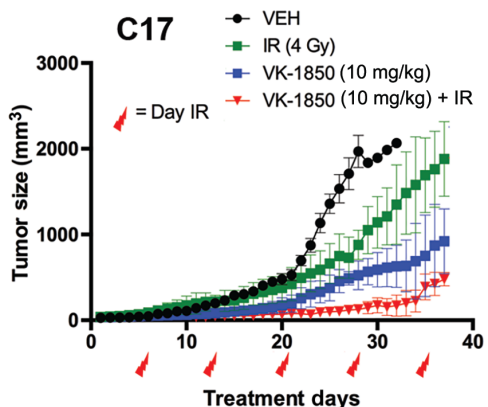
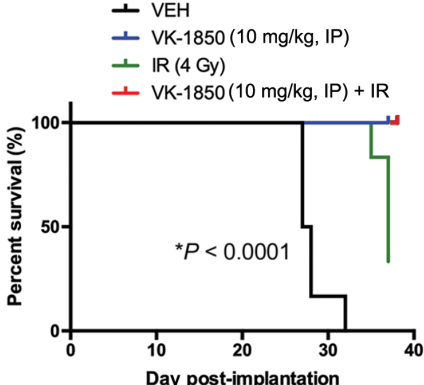
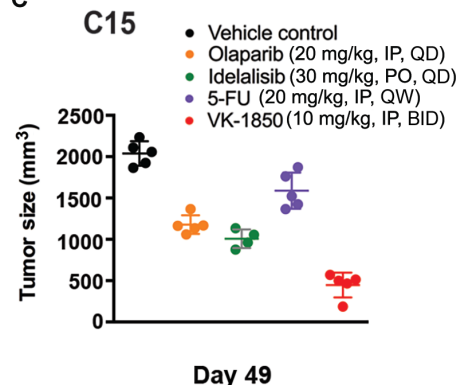
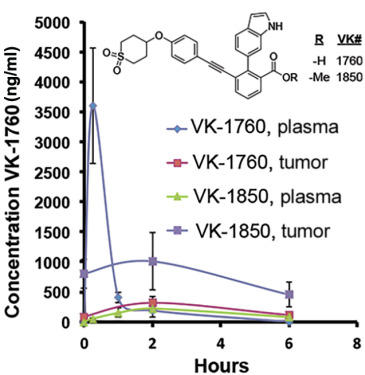
A**B****C****D**

Fig. 6. Comparison of EBNA1 inhibitors with other treatments. (A) C17-PDX was treated with vehicle (VEH) (black), IR (4 Gy) (green), VK-1850 (10 mg/kg) (blue), or a combination of IR and VK-1850 (red). IR was given on days 7, 14, 21, 28, and 35. (B) Survival curve for mice treated as described in (A) ($P = 0.0001$, log-rank Mantel-Cox test). (C) C15-PDX was treated with vehicle (black), olaparib (20 mg/kg, intraperitoneally) (yellow), idelalisib [30 mg/kg, orally (PO)] (green), 5-FU (20 mg/kg, intraperitoneally) (purple), or VK-1850 (10 mg/kg, intraperitoneally) (red). Tumor growth was assayed at day 49. QD, once daily; QW, once weekly. (D) Drug concentration (ng/ml) for VK-1760 in plasma or tumor at 0.5, 1, 2, and 5 hours after injection of VK-1760 (10 mg/kg) or the methyl ester prodrug VK-1850.

bound to DNA indicated that the carboxylic acid sterically interferes with DNA phosphate contacts. However, the primary interaction site 2 on EBNA1 is in a pocket adjacent to the main DNA interaction interface. The inhibitor binding site 2 on EBNA1 is centered around Thr⁵⁹⁰ and Asn⁵¹⁹, suggesting that inhibitors have allosteric effects on the EBNA1 N-terminal domain conformation associated with DNA binding. The change in N-terminal arm conformation is predicted from comparison of crystal structures of the apo and DNA-bound forms of EBNA1 (12, 13). This allosteric effect, which needs further biophysical confirmation, would explain how the EBNA1 inhibitors compete with higher-affinity DNA binding.

EBNA1 inhibitors were found to selectively block growth of EBV-positive cells in tissue culture and tumors *in vivo*. The most pronounced effect of EBNA1 inhibitors was on the rate of cell proliferation as measured by BrdU incorporation and metabolism as measured by resazurin assay. Long-term treatment revealed a reduction in viral DNA copy number and viral gene expression, as well as numerous changes in cellular gene expression correlating to pathways linked to apoptosis and cell cycle. Previous studies have shown that short-term short hairpin RNA (shRNA) depletion of

EBNA1 leads to a similar block to cellular proliferation (27). EBNA1 is known to bind to the EBV genome to regulate expression of viral genes, such as EBNA2 and LMP1, both of which are essential for B cell immortalization (7, 28). EBNA1 can also bind and regulate host genes that have critical functions in cell viability and have been implicated in tumorigenesis (7, 27). EBNA1 has additional activities, such as disruption of promyelocytic leukemia (PML) nuclear bodies and interactions with USP7 (11, 29, 30), that may contribute to its oncogenic functions, but it is unlikely that inhibitors of EBNA1 DNA binding affect these pathways. EBNA1 inhibitors led to the gradual loss of EBV DNA copy number, similar to that observed after chronic treatment with hydroxyurea (31, 32). Inhibition of EBNA1 DNA binding may function in a similar manner to hydroxyurea in preventing EBNA1 episome maintenance function but provides a more selective way to inhibit EBV-driven cellular proliferation and tumorigenesis.

There are several limitations to our findings. First, we do not fully understand the mechanism of action of EBNA1 inhibitors. Our results are consistent with the hypothesis that EBNA1 inhibitors block DNA binding, resulting in a reduction of EBV copy number and a decrease in host cell viability, but the mechanistic details remain to be elucidated. Second, as in many other cancer studies, we use xenograft studies in immunocompromised mice to assess the *in vivo* efficacy of

EBNA1 inhibitors. Xenograft studies often fail to represent the diversity and local tumor microenvironment of clinical disease. We offset some of these limitations by testing EBNA1 inhibitors using four different implanted cell lines, including two patient-derived tumor lines. These tumor/cell lines vary with respect to their origin, cell type, genetic background, latency program, and host mouse strain. Last, EBNA1 inhibitors appear to have an excellent safety profile, but a more comprehensive battery of *in vitro* and *in vivo* pharmacology studies, including genotoxicity and safety studies, is needed.

Long-term treatment of cells and tumors with EBNA1 inhibitors showed only modest signs of drug resistance. Cells derived from tumors treated for 1 month *in vivo* and 8 weeks in culture continued to respond to EBNA1 inhibitors as measured by proliferative index and metabolic activity. The amino acids comprising site 2 show no evidence for naturally occurring polymorphisms despite several other polymorphisms in EBNA1 DBD surface amino acids (33, 34). EBV tumors rarely lose EBV DNA and EBNA1 protein *in vivo*, and only one Burkitt LCL can be cured of EBV latency after prolonged treatment with hydroxyurea (31). This suggests that most EBV tumors and cell lines are highly dependent on EBNA1 and EBV

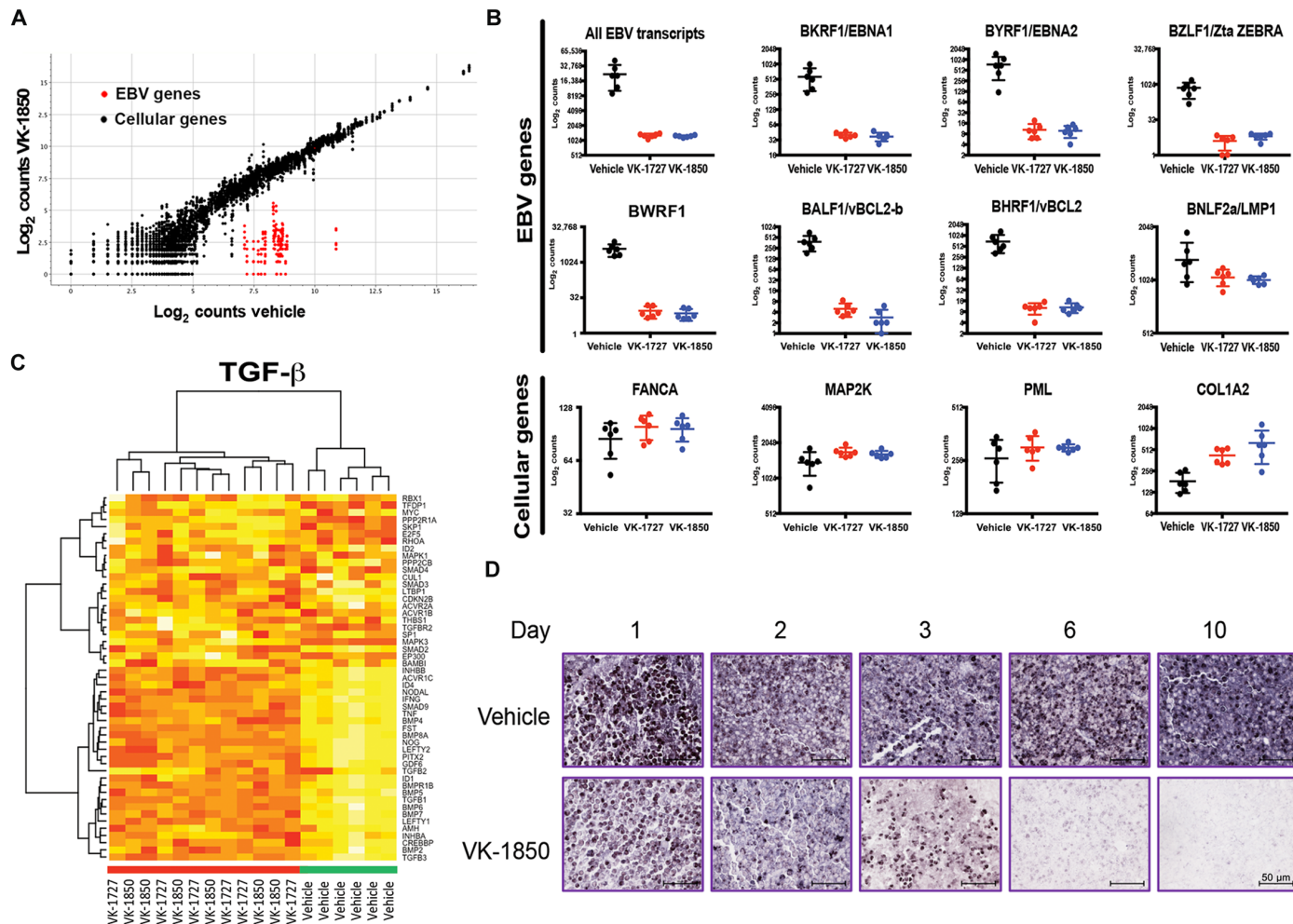


Fig. 7. EBV target engagement and cell survival pathways affected by EBNA1 inhibitors. (A) mRNA expression analysis comparing RNA expression in C15-PDX tumors treated with vehicle (x axis) and those treated with VK-1850 (y axis), shown as a scatter plot. EBV genes (red) are universally down-regulated in C15-PDX tumors isolated from animals treated with VK-1850 as compared to vehicle-treated animals. (B) mRNA expression of select EBV and cellular genes as measured by NanoString. EBV genes were significantly down-regulated for all EBV transcripts and specifically for *BKRF1*, *BYRF1*, *BZLF1*, *BWRF1*, *BALF*, *BHRF1*, and *BNLF* ($P < 0.001$) (ordinary one-way ANOVA) in C15-PDX tumors from VK-1727 (10 mg/kg; red) and VK-1850 (10 mg/kg; blue) mice as compared to vehicle-treated ones (black). The expression of most cellular genes was not significantly affected by treatment with EBNA1 inhibitors. For example, there was no significant change in the cellular genes *FANCA*, *MAP3K*, and *PML*. *COL1A2* mRNA expression was significantly increased ($P = 0.004$, ordinary one-way ANOVA) in EBNA1 inhibitor–treated cells. (C) Heat map analysis of cellular RNA expression of genes in the TGF-β pathway in tumors treated with vehicle, VK-1727, or VK-1850. Red indicates decreased expression, and yellow indicates increased expression. (D) Decreased EBER-ISH staining (purple) in tumors allowed to grow to 300 mm³ and then treated with VK-1850 or vehicle control for 1 to 10 days, as indicated. Scale bars, 50 μm.

episomes. The potential evolution of tumors to escape EBV dependence is plausible, and combinational therapies are likely to be required to prevent bypass mechanisms. We found that EBNA1 inhibitors are more efficacious in combination with radiation or cisplatin in treating NPC PDXs. Thus, EBNA1 inhibitors are likely to provide a clinical opportunity for early-stage monotherapy and late-stage combinatorial therapies to treat EBV-associated diseases.

MATERIALS AND METHODS

Study design

For animal studies

To determine sample size of the efficacy studies, we used power analysis to identify the number of animals required to obtain statistically significant results based on P values, using preliminary data generated

in the C666-1 model. The analysis accounted for the possible death of animals from causes not related to the study while at the same time reducing the total number of animals required. We performed pilot studies to provide estimates of the means and SDs required for a precise power calculation to indicate the likely response. To ensure the stringency of our blinded studies in the M14 lymphoma model, we used 10 mice per group. As we accumulated more data regarding the SD of the size of the tumors and average difference between the control and treated animals, we reassessed the number of animals to be used in later experiments. Accordingly, we brought the number of animals per group down to six animals per group to reach statistical significance for the NPC tumor models (C15-PDX and C17-PDX).

Data exclusions

Experiments with failed controls were excluded from consideration. Otherwise, all data were included.

Randomization

For C666-1 and A549 experiments, tumor-bearing mice were randomized into different treatment groups ($n = 8$) when the average tumor volume reached about 100 to 200 mm³. For C15- and C17-PDX experiments, tumors were measured 6 days after engraftment, and mice were grouped ($n = 6$ per group) so that the average tumor size was equivalent between groups. For M14 LCL experiments, tumors were measured by IVIS bioluminescent imaging 5 days after implantation, and mice were grouped ($n = 10$ per group) so that the average tumor size as measured by flux (photons/s) was equivalent across groups. After the mice were distributed into groups of 10, the investigators were blinded regarding which treatment (vehicle, VK-1850, or VK-1727) they were administering to the mice until after the study was completed, and all data points were collected and analyzed.

Blinding

Investigators were blinded to group allocation (vehicle versus EBNA1 inhibitors) while treating, imaging, weighing, and collecting tumor measurements for animal studies using the M14 LCL model.

EBNA1 DBD expression and purification

Residues 468 to 607 of B95.8 EBNA1 DBD were cloned into a modified pETDuet vector containing the *SMT3* gene, which encodes the yeast small ubiquitin-like modifier (SUMO) protein. The hexahistidine and SUMO protein tag were fused to the N terminus of the EBNA1 protein. *Escherichia coli* BL21(DE3) cells were transformed with plasmid, grown in the presence of ampicillin (100 µg/ml), and induced via autoinduction. Cell pellets were resuspended in 20 mM tris (pH 8.5), 1 M NaCl, 5 mM β-mercaptoethanol, 1 mM MgCl₂, 5 mM imidazole, 1 mM phenylmethylsulfonyl fluoride, and lysozyme (10 mg/ml). Cells were lysed by sonication at 4°C, and the insoluble fraction was separated by centrifugation at 18,000 rpm (SS-24 Sorvall) for 30 min. The soluble fraction was passed over pre-equilibrated Ni-NTA (nitritriacetic acid) resin (Qiagen) and washed with 20 mM tris (pH 8.5), 1 M NaCl, 5 mM β-mercaptoethanol, and 30 mM imidazole. Protein was batch eluted with 20 mM tris (pH 8.5), 1 M NaCl, 5 mM β-mercaptoethanol, and 300 mM imidazole. The protein was then concentrated and purified using a size exclusion column (HiLoad 26/60 Superdex 75; GE Life Sciences) pre-equilibrated with 20 mM tris (pH 8.5), 1 M NaCl, and 5 mM β-mercaptoethanol. This step also removed the imidazole. Fractions were collected, pooled, and incubated with His-SUMO1 protease (purified in-house). After cleavage, the mixture was passed over pre-equilibrated Ni-NTA resin and the flow-through was collected (His-SUMO, His-SUMO protease, and uncleaved fusion protein bound to the Ni-NTA resin). Cleaved EBNA1 was concentrated and purified using a size exclusion column (HiLoad 26/60 Superdex 75; GE Life Sciences) equilibrated with 1 mM Hepes (pH 7.2), 500 mM NaCl, and 10 mM dithiothreitol (DTT). Fractions were run on a bis-tris polyacrylamide gel to verify size and purity. Last, protein was pooled, concentrated to 10 to 20 mg/ml, aliquoted, and frozen at -80°C for long-term storage.

Crystallization, data collection, and analysis

Crystals were grown using the vapor diffusion method in 24 to 48 hours using purified EBNA1 (468 to 607) mixed 2 µl:2 µl with reservoir solution [50 mM MES (pH 6.5), 0 to 150 mM NaCl, and 10 mM DTT]. Crystals were transferred to a solution containing 25

to 30% glycerol and 0.2 µl of 50 mM pooled fragments and incubated for 4 to 8 hours. One hundred fragments were pooled in 20 different pools of five fragments each to maximize the likelihood of deconvolution. Data were collected on the X29 and X25 beamline at the National Synchrotron Light Source at Brookhaven National Laboratory (Upton, NY). Data were indexed, reduced, and scaled using HKL-3000. The structures were solved by isomorphous replacement. Models were refined in PHENIX using simulated annealing, minimization, and individual B-factor refinement. Between refinement cycles, the model was manually rebuilt using the program Coot. Data collection and refinement statistics are summarized in table S1.

ALPHA assay

An assay buffer of 25 mM tris (pH 7.5) (Fisher), 200 mM NaCl (Fisher), 1 mM MgCl₂ (Fisher), 0.01% CHAPS (Sigma-Aldrich), and 5 mM β-mercaptoethanol (Bio-Rad) was prepared. For EBNA1, 36 nM His-tagged protein (expressed and purified to >95% homogeneity) was incubated with Ni chelate acceptor beads (24 µg/ml) (PerkinElmer). Separately, 1.2 nM EBNA1 hairpin biotinylated DNA (5'-BtTGGGTAGCATATGCTATCTAGATAGCATATGCTAC-CC-3') (Integrated DNA Technologies) was incubated with streptavidin donor beads (24 µg/ml) (PerkinElmer) for 30 min at room temperature. In a 384-well microplate and under green light, 5 µl of protein/acceptor bead mix and 5 µl of DNA/donor bead mix were combined together in each well. Next, 150 nl of DMSO (Fisher Scientific)-dissolved compound was resuspended in 5 µl of assay buffer and then transferred into the wells. On the plate, columns 1, 2, 23, and 24 served as controls. The reaction mixture for columns 1 and 23 lacked DNA (negative control), and the reaction mixtures for columns 2 and 24 lacked compound (positive control). Plates were incubated in the dark for 1.5 to 2 hours, and then emission was measured (excitation, 680 nm; emission, 570 nm) using an EnVision XCite multilabel reader (PerkinElmer). For the LANA counterscreen, the assay was repeated using 45 nM His-tagged LANA protein (expressed and purified to >95% homogeneity) and 2.5 nM biotinylated DNA (5'-BtTCGGCCCCATGCCCGGGAGGCGCGCCTC-CCGCCCGGGCATGGGGCCG-3') (Integrated DNA Technologies).

HTRF assay

An assay buffer of 25 mM tris (pH 7.5), 200 mM NaCl, 1 mM MgCl₂, 0.01% CHAPS, and 5 mM β-mercaptoethanol was prepared. For EBNA1, 12 nM protein was incubated with anti-His d2 (225 ng/ml) (Cisbio). Separately, 1.2 nM EBNA1 hairpin DNA (described above) and sonicated salmon sperm DNA (12 µg/ml) were incubated with streptavidin-Tb (9.6 ng/ml) (Cisbio) for 30 min at room temperature. In a 384-well microplate, 5 µl of protein/anti-His d2 mix was added to each well. Similarly, 5 µl of DNA/streptavidin-Tb mix was added to each well. Then, 150 nl of DMSO-dissolved compound was resuspended in 5 µl of assay buffer and transferred into the wells. Similar to the ALPHA assay, columns 1, 2, 23, and 24 served as negative and positive controls. The reaction mixture for columns 1 and 23 lacked DNA (negative control), and the reaction mixtures for columns 2 and 24 lacked compound (positive control). Plates were incubated at room temperature for 1.5 to 2 hours and then measured with an EnVision XCite multilabel reader (PerkinElmer) using the ratiometric method (excitation, 335 nm; ratio of emission, 620 and 665 nm) according to the manufacturer's protocol (Cisbio). For the LANA counterscreen, the assay was repeated using 30 nM protein,

4.5 nM LANA hairpin DNA (described above), and sonicated salmon sperm DNA (36 µg/ml).

Heteronuclear single-quantum coherence nuclear magnetic resonance

To obtain ¹⁵N-labeled protein, bacterial cells harboring the His-SUMO-EBNA1 (459 to 607) plasmid were grown in the presence of ¹⁵NH₄Cl, vitamins, glucose, trace elements, and minimal M9 medium and induced by autoinduction as described above. Protein was purified as described above. 2D and 3D spectra were collected on 50 µM ¹⁵N-labeled EBNA1 protein sample using a 500-MHz Avance III Bruker NMR spectrometer with a cryoprobe. Additional HSQC spectra were collected with ligand additions of [50 µM] resuspended in deuterated DMSO-d₆. The spectra were overlaid, and the magnitude and specificity of the chemical shift perturbations were examined.

Surface plasmon resonance

Primary amine coupling of wild-type (EBV strain B95-8) EBNA1 DBD to a C5 Biacore sensor chip (GE Healthcare Life Sciences) had greatly reduced DNA activity (likely due to coupling of lysine residues that are important for DNA binding). As an alternative, we developed a thiol coupling method to immobilize EBNA1 on the Biacore sensor chip. We synthesized a construct that expressed a version of EBNA1 DBD (459 to 607) with the internal cysteines mutated to serine and Cys-Ala-Cys added to the C terminus. This version of EBNA1 DBD (EBNA1-CAC) was coupled to the C5 Biacore sensor chip [500 to 2000 response units (RUs)] and was confirmed to be capable of binding DNA. Binding between EBNA1 (0 to 200 nM) and compounds was performed in a buffer containing 50 mM tris (pH 7.5), 200 mM NaCl, 5 mM MgCl₂, 0.05% P20 surfactant, and 5% DMSO. Compound concentrations were run in random order on Biacore T200. Regeneration of the surface was ensured between binding events by washing with 50 mM tris (pH 7.5) and 1 M NaCl to remove all compounds. One cycle consisted of 60-s stabilization, 120-s injection, 90-s dissociation, and 60-s regeneration. Flow rate was constant at 30 µl/min. Resulting sensorgrams were used to obtain a K_d plot. Inhibitor binding to EBNA was fit for K_d (nM), R_{max} , and χ^2 using the Biacore T200 Evaluation Software (GE Healthcare Life Sciences). χ^2 less than 10% of R_{max} was deemed an acceptable dataset.

Isothermal titration calorimetry

For ITC experiments, 23.9 µM EBNA1 (468 to 607), dialyzed into a solution of 20 mM Hepes (pH 7.5), 250 mM NaCl, and 5 mM β-mercaptoethanol, was injected into the sample cell. The EBNA1 inhibitor VK-1248 was lyophilized and resuspended in the same dialysis buffer at a final concentration of 25 mM. Fifteen 2.5-µl injections containing DMSO and VK-1248 were titrated in an iTC200 instrument (Malvern Instruments) at 25°C to obtain a raw thermogram. The binding isotherm was calculated from the integrated thermogram fit using the one-site model in the Origin software. From the Origin software, using the one site binding model, $n = 1.10 \pm 0.06$, $K_D = 1.4 \pm 3.0$ µM, $\Delta H = -31.5 \pm 2.3$ kcal/mol, and $\Delta S = 6.7$ cal/mol per degree.

Chemistry

¹H NMR and ¹³C NMR spectra were obtained on a Varian Mercury NMR at 300 and 75 MHz, respectively. Purity (%) and mass spectral data were determined with a Waters Alliance 2695 high-performance

liquid chromatography–mass spectrometer (HPLC-MS) (Waters Symmetry C18, 4.6 × 75 mm, 3.5 µm) with a 2996 diode array detector from 210 to 400 nm equipped with a Micromass ZQ mass spectrometer and an electrospray ionization detector. High-resolution mass spectrometry (HRMS) analysis was carried out at the University of Notre Dame Mass Spectrometry and Proteomics Facility using a Bruker micrOTOF II. Preparative HPLC purifications were performed on a Gilson preparative HPLC with a Phenomenex Luna 5 µm C18 column, 150 × 21.2 mm, using a gradient of 5 to 95% acetonitrile in water (with 0.1% trifluoroacetic acid) over 15 min. Methods of chemical synthesis are described in the Supplementary Materials.

Cell-based assays

Resazurin cell respiration assay

Cells were plated at 1000 cells (in 50 µl) per well in a 384-well plate. Inhibitors were added 24 hours later over a 10-point concentration range with twofold dilutions (0.1953 to 100 µM). As positive and negative controls, cells in columns 1 and 23 were treated with DMSO alone (0.4%) and columns 2 and 24 were treated with puromycin (20 µg/ml). After 72 hours, resazurin (5 µl, final 50 µM) was added to each well. After 6 hours, plates were read on a PerkinElmer EnVision XCite multilabel plate reader (excitation, 560 nM; emission, 590 nM).

Plasmid replication

HeLa, 293T, or SUNE1 (~1 × 10⁶ cells) were plated in 10-cm dishes. Twenty-four hours later, cells in Dulbecco's minimum essential medium (1 to 10% fetal bovine serum) were transfected with Lipofectamine 2000 (12 µl; Invitrogen) and 4 µg of OriP plasmids expressing either FLAG-B95-8 EBNA or HA-B95-8 EBNA1. About 5 hours after transfection, fresh medium containing compound (10 to 15 µM) was added. Forty-eight hours after transfection, cells were split into 15-cm dishes with fresh compound and then harvested at 72 hours after transfection for both episomal DNA and protein. Episomal DNA was extracted by Hirt lysis (35). The DNA pellets were dissolved in 150 µl of H₂O or 10 mM tris-HCl and 1 mM EDTA buffer (pH 7.6), and 15 µl was subjected to restriction digestion with Bam HI alone, whereas 135 µl was subjected to Bam HI and Dpn I digestion overnight at 37°C. Pure DNA was extracted with phenol/chloroform (1:1), precipitated, electrophoresed on a 0.9% agarose gel, and transferred to a nylon membrane (PerkinElmer) for Southern blotting. Blots were visualized and quantified using a Typhoon 9410 phosphorimager (GE Healthcare).

BrdU proliferation assay

Cells were plated at 5 × 10⁴ per well (in 200 µl) in a 96-well plate and treated with DMSO alone (0.4%), VK-1727 (0.25 or 2.5 µM), or VK-1850 (0.25 or 2.5 µM). At 24 and 48 hours after treatment, the plates were centrifuged at 1000 rpm for 5 min, and the medium was carefully aspirated and replaced with fresh medium containing DMSO alone or EBNA1 inhibitor at the appropriate concentration. After 72 hours, a BrdU cell proliferation assay was performed according to the manufacturer's instructions (CytoSelect BrdU Cell Proliferation ELISA Kit, Cell Biolabs Inc.). Briefly, 10 µl of a 10× BrdU solution (100 µM BrdU) was added to each well, and plates were incubated at 37°C. Three hours later, cells were centrifuged at 1000 rpm for 5 min, washed thrice with 100 µl of phosphate-buffered saline (PBS), and treated with fix/denature solution. Cells were subsequently incubated with 100 µl of anti-BrdU antibody for 1 hour. Cells were washed thrice in 1× wash buffer, and after incubation with a secondary HRP-conjugated antibody, a substrate solution

was applied. Plates were read on a PerkinElmer EnVision XCite multilabel plate reader (absorbance, 450 nm).

ChIP assay

EBV-positive C666-1 cells were treated with indicated compounds at 30 μ M for indicated times, and medium with compounds was changed every 24 hours. Formaldehyde was used to cross-link the proteins to the DNA, and the cross-linking was stopped with glycine. Cells were washed three times with cold PBS and resuspended in ChIP lysis buffer. Sonication was used to shear DNA to lengths between 500 and 1000 base pairs by using a Branson Bioruptor. A rabbit anti-EBNA1 antibody (2 μ g per reaction) was used in immunoprecipitation. After washing, eluting, and decrosslinking, DNA was precipitated and purified by using a Qiagen PCR (polymerase chain reaction) purification kit. Real-time quantitative PCR (ABI 7900HT Fast Real-Time PCR System; Applied Biosystems) was performed to quantitate two EBV loci (DS50 and Qp) and one cellular locus (PITPNB), which have been reported to associate with EBNA1 protein in vivo (2, 3). OriLyt locus, which does not bind to EBNA1 protein in vivo, was used as a negative control. Primers are listed in table S2.

EBV viral DNA copy number

Viral loads were calculated by standard curve comparison with DNA from the Namalwa cell line (American Type Culture Collection), which contains two integrated copies of the EBV genome on chromosome 1, using primers for EBNA1 DNA sequence (table S2) (36).

Mouse studies

Ethics statement

All animal experiments were conducted under The Wistar Institute's approved Institutional Animal Care and Use Committee protocol no. 112320 (for M14 LCL; Luc⁺, experiments) or no. 112630 (for C15- and C17-PDX experiments) or the Anthem Biosciences Institutional Animal Ethics committee (IAEC) in accordance with the Committee for the Purpose of Control and Supervision of Experiments on Animals guidelines for animal experimentation ABD/IAEC/PR/25 R4–14–15 and ABD/IAEC/PR/25 R5–15–16. All mice in this study were managed in accordance with the National Institutes of Health (NIH) Office of Laboratory Animal Welfare ("PHS Policy on the Humane Care and Use of Research Animals"), the recommendations of the AAALAC (*The Guide for the Care and Use of Laboratory Animals*, 8th edition), and the standards recommended by the United Kingdom's National Centre for the Replacement, Refinement, and Reduction (NC3R) of Animals in Research ("Responsibility in the Use of Animals in Bioscience Research").

Mice

For experiments using the lymphoma model (M14 LCL; GFP⁺Luc⁺), NSG (NOD.Cg-*Prkdc*^{scid}/*Il2rg*^{tm1Wjl}/ScJ; <https://www.jax.org/search?q=0005557>) mice were bred in-house at The Wistar Institute under protocol no. 112092. Athymic Swiss nude mice (strain 490, homozygous) were purchased from Charles River Laboratories for all experiments using the NPC C15- and C17-PDX tumors. Experiments using NPC (C666-1) and lung carcinoma cell lines (A549) were performed with C.B-*Igh-1b*/GbmsTac-*Prkdc*^{scid}-*Lyst*^{bg} N7 purchased from Taconic. All mice were enrolled in their respective studies at 6 to 8 weeks of age and housed in micro-isolator cages in a designated, specific pathogen-free facility at either The Wistar Institute (Philadelphia, PA) or Anthem Biosciences (Bengaluru, Karnataka, India), where they were fed sterile food and water ad libitum. Mice were euthanized via CO₂ administration according to the American Association for Accreditation of Laboratory Animal Care (AAALAC) euthanasia guidelines.

Tumor implantation, grouping, and equalization

For cell line experiments (M14 LCL, C666-1, and A549), mice were anesthetized using isoflurane and engrafted with a cell suspension (>98% viability) of 1×10^6 M14 LCL, 5×10^6 C666-1, or 5×10^6 A549 cells resuspended in 1× PBS (pH 7.4) and mixed with 20% of cold Matrigel (Corning Life Sciences) and maintained on ice. Cells were injected subcutaneously into the flank of each animal using a 22-gauge needle. For C15- and C17-PDX experiments, mice were anesthetized and 4×10 mm³ pieces of C15-PDX or C17-PDX tumors were surgically implanted subcutaneously as previously described (18). Animals were weighed, monitored, and measured for palpable tumors and tumor growth daily. All tumors were measured by caliper, and tumor volume was calculated as follows: tumor volume = [length (L) × width (W)²]/2. For C666-1 and A549 experiments, tumor-bearing mice were randomized into different treatment groups ($n = 8$) when the average tumor volume reached about 100 to 200 mm³. For C15- and C17-PDX experiments, tumors were measured 6 days after engraftment and mice were grouped ($n = 6$ per group) so that the average tumor size was equivalent between groups. For M14 LCL experiments, tumors were measured by IVIS bioluminescent imaging 5 days after implantation and mice were equalized ($n = 10$ per group) so that the average tumor size as measured by flux (photons/s) was equivalent across groups. After the mice were distributed into groups of 10, the investigators were blinded regarding which treatment (vehicle, VK-1850, or VK-1727) they were administering to the mice until after the study was completed and all data points were collected and analyzed.

Compound formulation and treatment schedules

Compounds were weighed and transferred to graduated tubes, and formulation reagents were added slowly dropwise in the following order: 3.5% Tween 80 (Sigma), 5% dimethylacetamide (Sigma), 20% PEG400 (polyethylene glycol, molecular weight 400) (Sigma), 20% propylene glycol, 35% PBS, and 16.5% water. The vehicle control contained formulation reagents without the compounds. Formulated compounds were filter-sterilized and administered intraperitoneally twice daily at 10 to 40 mg/kg in a dose volume of 10 ml/kg body weight.

Visualization and quantitation of M14 LCL (Luc⁺) tumor growth using the Xenogen IVIS Bioluminescent Imaging System

Mice were intraperitoneally injected with luciferin (Gold Biotechnology) at a dose of 15 mg/kg in a dose volume of 10 ml/kg body weight 15 min before imaging; this was the optimal interval between luciferase injection and bioluminescent imaging determined by photon flux. Mice were anesthetized using isoflurane before imaging, which was performed twice per week. Flux (photons/s) and radiance (photons s⁻¹ cm⁻²) were determined using the IVIS imaging software.

Combination drug and radiation treatment

For radiation studies, mice were implanted with C17-PDX as described and treated every 7 days with a sublethal dose (4 Gy) administered using a traditional cesium-137 source. For studies involving other drugs, mice were implanted with C15-PDX as described. 5-FU (Sigma-Aldrich), olaparib (O-9201; LC Laboratories), and VK-1850 were weighed and transferred to graduated tubes, and formulation reagents were added slowly dropwise in the following order: 3.5% Tween 80 (Sigma), 5% dimethylacetamide (Sigma), 20% PEG400 (Sigma), 20% propylene glycol, 35% PBS, and 16.5% water. Formulated compounds were filter-sterilized. VK-1850 was administered intraperitoneally twice daily; olaparib (20 mg/kg) was administered

intraperitoneally once daily; 5-FU (20 mg/kg) was administered intraperitoneally once weekly. Idelalisib (I-7447; LC Laboratories) was weighed, transferred to a graduated tube, and formulated with 2.5% Tween 80 (Sigma) and 97.5% of a 0.5% carboxymethyl cellulose solution and administered orally once daily at a concentration of 30 mg/kg in a dose volume of 10 ml/kg body weight. The vehicle control consisted of formulation reagents without compound. All animals receiving drugs administered intraperitoneally also received the oral vehicle formulation once daily; animals treated with idelalisib also received the intraperitoneal vehicle formulation twice daily.

Gene expression analysis (NanoString)

C15-PDX tumor sections were flash-frozen, and later, RNA was isolated using the RNeasy Mini Kit (Qiagen) and treated with deoxyribonuclease (Qiagen). Gene expression analysis and data processing were performed in the nCounter system according to the manufacturer's instructions and nSolver 3.0 software (NanoString Technologies). The human nCounter PanCancer Pathways Panel was used and supplemented with a codeset designed to detect 30 EBV-encoded RNAs (*BALF1/vBCL2-b*, *BALF2/DNA binding protein*, *BALF5/DNA polymerase*, *BBLF4/helicase*, *BCRF1/vIL-10*, *BDFL3/gp150*, *BERF1/EBNA3A*, *BERF2/EBNA3B*, *BERF4/EBNA3C*, *BFLF2/capsid*, *BGLF2*, *BGLF4/protein kinase*, *BGRF1/terminase*, *BHLF1*, *BHRF1/bcl-2*, *BKRF1/EBNA1*, *BKRF3/uracil DNA glycosylase*, *BMRF1/processivity*, *BNLF2a/LMP1*, *BNRF1/vFGARAT*, *BORF2/ribonucleotide reductase*, *BSLF1/primase*, *BVLF1/late gene regulator*, *BVRF2/protease*, *BWRF1*, *BXLF1/TK*, *BYRF1/EBNA2*, *BZLF1/Zta ZEBRA*, *BCLF1/capsid*, and *LMP2A/terminal proteins*). Data were normalized using housekeeping genes selected by the nSolver 3.0 software (*EIF2B4*, *HDAC3*, *SF3AC*, *AGK*, and *USP39*).

Epstein-Barr-encoded RNA *in situ* hybridization

Tumor sections were fixed in neutral buffered formalin solution (10%; Sigma) overnight at room temperature before paraffin embedding. The EBER-ISH assay was performed using the EBER PNA Probe/Fluorescein and the One-Day In Situ Hybridization Procedure for RNA Detection Using PNA Probes, per the manufacturer's instructions (Dako).

Statistical analysis

For high-throughput biochemical and cell-based assays, percent inhibition was calculated for each inhibitor using an average of the positive and negative control columns as the high and low values, respectively, as follows: Percent inhibition = $[1 - (N - \text{Low}) / (\text{High} - \text{Low})] \times 100\%$, where N is the average value for each inhibitor, Low is puromycin-treated, and High is no treatment. Plate uniformity and reproducibility were assessed, and plate performance characteristics were calculated (Z-score, minimum significant ratio, limits of agreement). IC₅₀/EC₅₀ values were calculated by Dotmatics using a relative four-parameter logistic model corresponding to a response midway between the estimates of the lower and upper plateaus. Statistics for Figs. 2 to 4 and figs. S7 and S8 were performed in GraphPad Prism 6. For ChIP, BrdU incorporation, plasmid replication assays, and animal studies, P values were determined by two-tailed Student's t test for three experimental or biological replicates.

Software

NanoString data were analyzed using the nSolver 3.0 package. GraphPad Prism 6 was used for generating graphs in Figs. 2 to 4 and figs. S7 and S8.

SUPPLEMENTARY MATERIALS

www.scientifictranslationalmedicine.org/cgi/content/full/11/482/eaau5612/DC1

Materials and Methods

- Fig. S1. Cocrystal structure of merged fragment, VK-0497, in site 2 of EBNA1.
- Fig. S2. Cocrystal structure of VK-0941 bound in site 2 of EBNA1.
- Fig. S3. Cocrystal structure of VK-1760 bound to EBNA1.
- Fig. S4. Biacore sensorgrams of EBNA1-CAC with EBNA1 inhibitors.
- Fig. S5. Biacore sensorgrams of EBNA1-CAC with VK-1760.
- Fig. S6. HSQC NMR spectra with ¹⁵N-labeled EBNA1.
- Fig. S7. Cell viability assays of VK-1850.
- Fig. S8. Cell-based activity assay of acid compounds.
- Fig. S9. Combination treatment of C17-PDX with VK-1850 and IR.
- Fig. S10. Combination treatment of C15-PDX and C17-PDX with EBNA1 inhibitor and cisplatin.
- Fig. S11. Plasma and tumor concentrations of VK-1850.
- Fig. S12. Assay for drug resistance in cells treated long-term with EBNA1 inhibitors.
- Fig. S13. Heat map analysis of cellular gene expression using the NanoString Tumor Progression Panel.
- Fig. S14. Synthesis of VK-0497.
- Fig. S15. Synthesis of 3-ethynyl-2-(1*H*-indol-6-yl)-benzoic acid methyl ester.
- Fig. S16. Chemical structure of VK-1850.
- Table S1. Data collection and refinement statistics of EBNA1 cocrystal structures.
- Table S2. Primers for quantitative PCR DNA copy and ChIP assay.
- Data file S1. Original data for Fig. 3B.
- Data file S2. Original data for fig. S8B.
- Data file S3. Original data for Fig. 3E.
- Data file S4. Original data for Fig. 3G.
- Data file S5. Original data for fig. S12A.
- Data file S6. Original data for fig. S12B.
- Data file S7. Custom NanoString CodeSet sequences for EBV.
- Data file S8. Changes in gene expression after treatment with VK-1850 and VK-1727.

REFERENCES AND NOTES

- D. M. Parkin, Global cancer statistics in the year 2000. *Lancet Oncol.* **2**, 533–543 (2001).
- L. S. Young, L. F. Yap, P. G. Murray, Epstein–Barr virus: More than 50 years old and still providing surprises. *Nat. Rev. Cancer* **16**, 789–802 (2016).
- L. S. Young, A. B. Rickinson, Epstein–Barr virus: 40 years on. *Nat. Rev. Cancer* **4**, 757–768 (2004).
- M.-S. Kang, E. Kieff, Epstein–Barr virus latent genes. *Exp. Mol. Med.* **47**, e131 (2015).
- P. J. Farrell, Epstein–Barr virus and cancer. *Annu. Rev. Pathol.* **24**, 29–53 (2019).
- L. Frappier, Ebna1. *Curr. Top. Microbiol. Immunol.* **391**, 3–34 (2015).
- D. W. Smith, B. Sugden, Potential cellular functions of Epstein–Barr nuclear antigen 1 (EBNA1) of Epstein–Barr virus. *Viruses* **5**, 226–240 (2013).
- D. R. Rawlins, G. Milman, S. D. Hayward, G. S. Hayward, Sequence-specific DNA binding of the Epstein–Barr virus nuclear antigen (EBNA-1) to clustered sites in the plasmid maintenance region. *Cell* **42**, 859–868 (1985).
- J. L. Yates, N. Warren, B. Sugden, Stable replication of plasmids derived from Epstein–Barr virus in various mammalian cells. *Nature* **313**, 812–815 (1985).
- E. R. Leight, B. Sugden, EBNA-1: A protein pivotal to latent infection by Epstein–Barr virus. *Rev. Med. Virol.* **10**, 83–100 (2000).
- L. Frappier, Contributions of Epstein–Barr nuclear antigen 1 (EBNA1) to cell immortalization and survival. *Viruses* **4**, 1537–1547 (2012).
- A. Bochkarev, J. A. Barwell, R. A. Pfuetzner, E. Bochkareva, L. Frappier, A. M. Edwards, Crystal structure of the DNA-binding domain of the Epstein–Barr virus origin-binding protein, EBNA1, bound to DNA. *Cell* **84**, 791–800 (1996).
- A. Bochkarev, J. A. Barwell, R. A. Pfuetzner, W. Furey Jr., A. M. Edwards, L. Frappier, Crystal structure of the DNA-binding domain of the Epstein–Barr virus origin-binding protein EBNA 1. *Cell* **83**, 39–46 (1995).
- C. W. Murray, D. C. Rees, The rise of fragment-based drug discovery. *Nat. Chem.* **1**, 187–192 (2009).
- M. C. Smith, J. E. Gestwicki, Features of protein–protein interactions that translate into potent inhibitors: Topology, surface area and affinity. *Expert Rev. Mol. Med.* **14**, e16 (2012).
- P. Lassalas, B. Gay, C. Lasfargeas, M. J. James, V. Tran, K. G. Vijayendran, K. R. Brunden, M. C. Kozlowski, C. J. Thomas, A. B. Smith III, D. M. Huryn, C. Ballatore, Structure property relationships of carboxylic acid isosteres. *J. Med. Chem.* **59**, 3183–3203 (2016).
- J. B. Zawilska, J. Wojcieszak, A. B. Olejniczak, Prodrugs: A challenge for the drug development. *Pharmacol. Rep.* **65**, 1–14 (2013).
- P. Busson, G. Ganem, P. Flores, F. Mugneret, B. Clausse, B. Caillou, K. Braham, H. Wakasugi, M. Lipinski, T. Tursz, Establishment and characterization of three transplantable EBV-containing nasopharyngeal carcinomas. *Int. J. Cancer* **42**, 599–606 (1988).

19. S. T. Cheung, D. P. Huang, A. B. Y. Hui, K. W. Lo, C. W. Ko, Y. S. Tsang, N. Wong, B. M. Whitney, J. C. K. Lee, Nasopharyngeal carcinoma cell line (C666-1) consistently harbouring Epstein-Barr virus. *Int. J. Cancer* **83**, 121–126 (1999).
20. A. W. M. Lee, W. T. Ng, Y. H. Chan, H. Sze, C. Chan, T. H. Lam, The battle against nasopharyngeal cancer. *Radiat. Oncol.* **104**, 272–278 (2012).
21. M. Nasimuzzaman, M. Kuroda, S. Dohno, T. Yamamoto, K. Iwatsuki, S. Matsuzaki, R. Mohammad, W. Kumita, H. Mizuguchi, T. Hayakawa, H. Nakamura, T. Taguchi, H. Wakiguchi, S. Imai, Eradication of Epstein-Barr virus episome and associated inhibition of infected tumor cell growth by adenovirus vector-mediated transduction of dominant-negative EBNA1. *Mol. Ther.* **11**, 578–590 (2005).
22. M. Hong, Y. Murai, T. Kutsuna, H. Takahashi, K. Nomoto, C.-M. Cheng, S. Ishizawa, Q.-L. Zhao, R. Ogawa, B. V. Harmon, K. Tsuneyama, Y. Takano, Suppression of Epstein-Barr nuclear antigen 1 (EBNA1) by RNA interference inhibits proliferation of EBV-positive Burkitt's lymphoma cells. *J. Cancer Res. Clin. Oncol.* **132**, 1–8 (2006).
23. Q. Yin, E. K. Flemington, siRNAs against the Epstein Barr virus latency replication factor, EBNA1, inhibit its function and growth of EBV-dependent tumor cells. *Virology* **346**, 385–393 (2006).
24. A. Yasuda, K. Noguchi, M. Minoshima, G. Kashiwazaki, T. Kanda, K. Katayama, J. Mitsuhashi, T. Bando, H. Sugiyama, Y. Sugimoto, DNA ligand designed to antagonize EBNA1 represses Epstein-Barr virus-induced immortalization. *Cancer Sci.* **102**, 2221–2230 (2011).
25. D. T. Vereide, B. Sugden, Lymphomas differ in their dependence on Epstein-Barr virus. *Blood* **117**, 1977–1985 (2011).
26. E. K. Lee, S. Y. Kim, K.-W. Noh, E. H. Joo, B. Zhao, E. Kieff, M.-S. Kang, Small molecule inhibition of Epstein-Barr virus nuclear antigen-1 DNA binding activity interferes with replication and persistence of the viral genome. *Antiviral Res.* **104**, 73–83 (2014).
27. I. Tempera, A. De Leo, A. V. Koskenkov, M. Cesaroni, H. Song, N. Dawany, L. Showe, F. Lu, P. Wikramasinghe, P. M. Lieberman, Identification of *MEF2B*, *EBF1*, and *IL6R* as direct gene targets of Epstein-Barr virus (EBV) nuclear antigen 1 critical for EBV-infected B-lymphocyte survival. *J. Virol.* **90**, 345–355 (2016).
28. M. Altmann, D. Pich, R. Ruiss, J. Wang, B. Sugden, W. Hammerschmidt, Transcriptional activation by EBV nuclear antigen 1 is essential for the expression of EBV's transforming genes. *Proc. Natl. Acad. Sci. U.S.A.* **103**, 14188–14193 (2006).
29. L. Frappier, Viral disruption of promyelocytic leukemia (PML) nuclear bodies by hijacking host PML regulators. *Virulence* **2**, 58–62 (2011).
30. M. N. Holowaty, M. Zeghouf, H. Wu, J. Tellam, V. Athanasopoulos, J. Greenblatt, L. Frappier, Protein profiling with Epstein-Barr nuclear antigen-1 reveals an interaction with the herpesvirus-associated ubiquitin-specific protease HAUSP/USP7. *J. Biol. Chem.* **278**, 29987–29994 (2003).
31. J. Chodosh, V. P. Holder, Y.-J. Gan, A. Belgaumi, J. Sample, J. W. Sixbey, Eradication of latent Epstein-Barr virus by hydroxyurea alters the growth-transformed cell phenotype. *J. Infect. Dis.* **177**, 1194–1201 (1998).
32. K. S. Slobod, G. H. Taylor, J. T. Sandlund, P. Furth, K. J. Helton, J. W. Sixbey, Epstein-Barr virus-targeted therapy for AIDS-related primary lymphoma of the central nervous system. *Lancet* **356**, 1493–1494 (2000).
33. S. Correia, A. Palser, C. Elgueta Karstegl, J. M. Middeldorp, O. Ramayanti, J. I. Cohen, A. Hildesheim, M. D. Fellner, J. Wiels, R. E. White, P. Kellam, P. J. Farrell, Natural variation of Epstein-Barr virus genes, proteins, and primary MicroRNA. *J. Virol.* **91**, e00375–17 (2017).
34. J. Dheekollu, K. Malecka, A. Wiedmer, H.-J. Delecluse, A. K. S. Chiang, D. C. Altieri, T. E. Messick, P. M. Lieberman, Carcinoma-risk variant of EBNA1 deregulates Epstein-Barr virus episomal latency. *Oncotarget* **8**, 7248–7264 (2017).
35. B. Hirt, Selective extraction of polyoma DNA from infected mouse cell cultures. *J. Mol. Biol.* **26**, 365–369 (1967).
36. Y. M. D. Lo, L. Y. S. Chan, K.-W. Lo, S.-F. Leung, J. Zhang, A. T. C. Chan, J. C. K. Lee, N. M. Hjelm, P. J. Johnson, D. P. Huang, Quantitative analysis of cell-free Epstein-Barr virus DNA in plasma of patients with nasopharyngeal carcinoma. *Cancer Res.* **59**, 1188–1191 (1999).
- Cancer Center Core Grant P30 CA010815-47). J.S.D. was supported by Wistar training grant T32 CA09171. **Author contributions:** T.E.M. was responsible for study design, implementation of a fragment-based approach, multisite coordination of the EBNA1 inhibitor program, and experiments (x-ray crystallography; Figs. 1, A to C, and 2A; figs. S1 to S3; and table S1). He also participated in the writing and preparation of the manuscript. G.R.S. was responsible for study design, multisite coordination of the EBNA1 inhibitor program, medicinal chemistry, and compound synthesis. S.S.S. participated in study design and the following experiments: proliferation assays (Fig. 3B and figs. S8B and S12A), mouse studies (Figs. 4, A to C and E to I, and 6, A to D, and figs. S9 and S10), viral and cellular gene expression studies (NanoString experiments and analysis and EBER-ISH; Fig. 7, A to D, and fig. S13, A to E), and preliminary drug resistance studies (fig. S12, A and B). She also participated in the writing and preparation of the manuscript. M.E.M. was responsible for medicinal chemistry and compound synthesis. J.S.D. was responsible for the study design and execution of cell-based studies including the proliferation assays (Fig. 3B and figs. S8B and S12A), the resazurin cell viability assays (Fig. 3C and figs. S7 and S8C), and the replication maintenance assay (Fig. 3, D to F). She also participated in the writing and preparation of the manuscript. K.A.M. performed x-ray crystallography (Figs. 1, A to C, and 2A; figs. S1 to S3; and table S1), ITC studies (Fig. 2C), and biacore experiments (figs. S4 and S5). L.T. participated in the following experiments: the ALPHA assay (Fig. 1D) and mouse studies (Figs. 4, A to C and E to I, and 6, A to D, and figs. S9 and S10). She also participated in the writing and preparation of the manuscript. A.P.J.v.d.H. participated in study design for cell-based assays (Fig. 3). B.-W.G. participated in study design for cell-based assays (Fig. 3) and performed the ChIP assay and analysis (Fig. 3G). J.A.C. developed and performed the ALPHA assay (Fig. 1C) and the resazurin cell viability assay (Fig. 3C). D.H.T. participated in the ALPHA assay (Fig. 1C) and the resazurin cell viability assay (Fig. 3C). B.R.W. participated in mouse studies (Figs. 4, A to C and E to I, and 6, A to D, and figs. S9 and S10) and viral and cellular gene expression studies (NanoString experiments and analysis and EBER-ISH) (Fig. 7, A to D, and fig. S13, A to E). Y.Z. participated in compound synthesis. V.V. was responsible for overseeing compound manufacture and animal studies (Figs. 4D and 5, A and B, and fig. S11) at Anthem. E.R.Z. performed the HSQC NMR experiment (Fig. 2D and fig. S6). P.B. participated in study design, PDX transfer, and selection of key reagents. A.B.R. was responsible for overseeing medicinal chemistry and compound synthesis. P.M.L. was responsible for study design, implementation of a fragment-based approach, multisite coordination of the EBNA1 inhibitor program, and the overall scientific direction of the EBNA1 inhibitor project. He was the principal author of the manuscript and led its preparation. **Competing interests:** The Wistar Institute on behalf of the authors T.E.M. and P.M.L. have filed patent applications PCT/US14/65765 “EBNA1 inhibitors and their method of use” and PCT/US2016/032574 “EBNA1 inhibitors and methods using same” covering composition of matter and their use on the small molecules disclosed here for the treatment of human cancer and other diseases. Wistar, T.E.M. and P.M.L., and Fox Chase Chemical Diversity Center Inc. (FCCDC) have received financial benefit from the license to Cullinan Apollo Corp. and would receive additional financial benefit should the development of the EBNA1 inhibitor meet certain milestones including commercialization. A.P.J.v.d.H., M.E.M., B.-W.G., and J.A.C. were employed by Vironika LLC. P.M.L. is the owner of Vironika LLC. G.R.S., M.E.M., Y.Z., V.V., and A.B.R. are employees of FCCDC. A.B.R., M.E.M., and Y.Z. have ownership interests in the company (FCCDC). B.-W.G. is currently employed by WuXi AppTech. A.P.J.v.d.H., K.A.M., D.H.T., and L.T. are currently employees of Johnson & Johnson. V.V. is currently an employee of Senseonics. J.A.C. is currently an employee of The Wistar Institute. E.R.Z. was a paid consultant on the project. E.R.Z. is currently an employee of Pfizer. **Data and materials availability:** All data associated with this study are present in the paper or Supplemental Materials. Compounds can be made available in limited supply through material transfer agreement with The Wistar Institute. All other reagents described are available upon request or can be purchased from vendors. Crystallographic data have been submitted to the Protein Data Bank (PDB) (RCSB.org) under PDB codes 6NPI (VK0044), 6NPM (VK0064), and 6NPP (VK-0497).

Submitted 22 June 2018

Accepted 7 February 2019

Published 6 March 2019

10.1126/scitranslmed.aau5612

Citation: T. E. Messick, G. R. Smith, S. S. Soldan, M. E. McDonnell, J. S. Deakyne, K. A. Malecka, L. Tolvinski, A. P. J. van den Heuvel, B.-W. Gu, J. A. Cassel, D. H. Tran, B. R. Wassermann, Y. Zhang, V. Velvadapu, E. R. Zartler, P. Busson, A. B. Reitz, P. M. Lieberman, Structure-based design of small-molecule inhibitors of EBNA1 DNA binding blocks Epstein-Barr virus latent infection and tumor growth. *Sci. Transl. Med.* **11**, eaau5612 (2019).

Acknowledgments: We would like to thank A. Mills-Duggan, G. Trainor, A. Rickinson, H. Steinman, M. Kates, P. Korytko, S. Chen, H. Song, and M. Carlsen. We would also like to thank the staff from the animal facility, imaging, genomics, bioinformatics, and molecular screening cores at The Wistar Institute. **Funding:** This work was supported by grants from the Wellcome Trust (Seeding Drug Discovery WT096496/Z/11/Z) and the NIH (R43AI079928, R43AI096588, and R44AI096588 to Vironika LLC; R01 CA093606 and R01 DE017336 to P.M.L.; and Wistar

Science Translational Medicine

Structure-based design of small-molecule inhibitors of EBNA1 DNA binding blocks Epstein-Barr virus latent infection and tumor growth

Troy E. Messick, Garry R. Smith, Samantha S. Soldan, Mark E. McDonnell, Julianna S. Deakyne, Kimberly A. Malecka, Lois Tolvinski, A. Pieter J. van den Heuvel, Bai-Wei Gu, Joel A. Cassel, Donna H. Tran, Benjamin R. Wassermann, Yan Zhang, Venkata Velvadapu, Edward R. Zartler, Pierre Busson, Allen B. Reitz and Paul M. Lieberman

Sci Transl Med **11**, eaau5612.
DOI: 10.1126/scitranslmed.aau5612

No holds Barr-ed for cancer treatment

Persistent latent infection with Epstein-Barr virus contributes to tumorigenesis in a variety of cancer types. The only viral protein that is consistently expressed in these tumors is Epstein-Barr nuclear antigen 1, which performs a variety of biological functions. To target this antigen, Messick *et al.* designed a series of chemical inhibitors and then tested them *in vitro* and in multiple mouse models of Epstein-Barr virus–associated cancer. The authors characterized the inhibitors using a variety of assays, examined the mechanism by which they work, and demonstrated preclinical effectiveness and suitable pharmacological properties, paving the way for further therapeutic development.

ARTICLE TOOLS

<http://stm.science.org/content/11/482/eaau5612>

SUPPLEMENTARY MATERIALS

<http://stm.science.org/content/suppl/2019/03/04/11.482.eaau5612.DC1>

RELATED CONTENT

<http://stm.science.org/content/scitransmed/3/107/107fs7.full>
<http://stm.science.org/content/scitransmed/6/242/242ra83.full>
<http://stm.science.org/content/scitransmed/10/447/eaar7223.full>
<http://stm.science.org/content/scitransmed/7/293/293ra104.full>

REFERENCES

This article cites 36 articles, 6 of which you can access for free
<http://stm.science.org/content/11/482/eaau5612#BIBL>

PERMISSIONS

<http://www.science.org/help/reprints-and-permissions>

Use of this article is subject to the [Terms of Service](#)

Science Translational Medicine (ISSN 1946-6242) is published by the American Association for the Advancement of Science, 1200 New York Avenue NW, Washington, DC 20005. 2017 © The Authors, some rights reserved; exclusive licensee American Association for the Advancement of Science. No claim to original U.S. Government Works. The title *Science Translational Medicine* is a registered trademark of AAAS.